Journal of Materials Chemistry A

ROYAL SOCIETY OF CHEMISTRY

PAPER

View Article Online
View Journal | View Issue

Cite this: J. Mater. Chem. A, 2024, 12, 4325

Disclosing the true atomic structure of {001} facets in shape-engineered TiO_2 anatase nanoparticles†

Stefano Pantaleone, [a] Francesco Pellegrino, [ab] Valter Maurino, [ab] Marta Corno, [a] Piero Ugliengo [a] and Lorenzo Mino *[a]

In the last decade shape-engineering of TiO_2 anatase nanoparticles (NPs) has attracted increasing attention owing to the possibility to maximize the presence of {001} facets, which have been reported to show peculiar adsorption, electronic, and (photo)catalytic properties. It is well-known that the anatase (001) surface is prone to reconstruction and several models have been proposed and validated by DFT calculations and single crystal studies. However, its true atomic structure in shape-engineered TiO_2 anatase nanoparticles often remains elusive. In this study we shed light on this issue combining IR spectroscopy of CO adsorbed at very low temperature and thorough DFT modelling. Our results show that the thermal treatment in oxygen, performed to remove the capping agents (*i.e.*, fluorides) employed in the synthesis of shape-controlled NPs, leads to a reconstruction of the {001} facets which is compatible with an "add-oxygen" model (AOM) and not with the most commonly reported "add-molecule" model (ADM). These findings can guide future experimental and computational studies highlighting that the AOM reconstruction is the most appropriate model to describe the properties and reactivity of the {001} facets in shape-controlled TiO_2 nanoparticles after thermal removal of fluorides.

Received 1st November 2023
Accepted 11th January 2024

DOI: 10.1039/d3ta06694k

rsc.li/materials-a

1. Introduction

Titanium dioxide (TiO_2) is a reducible metal oxide which has been, for many decades, the subject of thousands of scientific papers due to its widespread use in photocatalysis, lithium ion batteries and dye-sensitized solar cells.[1] In these applications the functional properties are, to a large extent, controlled by the TiO_2 surface chemistry.[2–4] Thus, increasing research efforts have been devoted to engineer the shape of titania nanoparticles (NPs) to tune their physicochemical properties and optimize their reactivity.[5,6] The usual equilibrium shape of TiO_2 anatase crystals is a truncated tetragonal bipyramid, mainly exposing the most stable {101} facets. Conversely, only a small fraction of the (001) surface is present owing to its high surface energy.[7] However, the latter surface has attracted great attention since the last decade for its supposed superior photocatalytic activity.[8–10]

The synthesis of TiO_2 "nano-sheets" (n-sh) with dominant {001} facets requires the use of suitable capping agents (usually fluoride ions), which are able to stabilize the (001) surface during the crystal growth.[11,12] Therefore, the surface of the NPs after the synthesis is terminated with Ti–F groups and F^- is also normally present in the bulk.[13–16] To completely remove these capping agents, the NPs are usually calcined at high temperature (generally between 773 and 873 K),[17–19] but this procedure can lead to a reconstruction of the unstable {001} facets, which can dramatically modify their functional properties.[19–21]

The reconstruction phenomenon has been widely investigated, employing both surface science techniques and density functional theory (DFT) calculations. It has been highlighted that the bulk truncated-(001) surface preferentially undergoes a 1×4 reconstruction during thermal treatments.[21] The dynamics of the reconstruction process has been recently studied in detail employing environmental transmission electron microscopy (ETEM) highlighting in real-time the transition from metastable 1×3 and 1×5 reconstructions to the most stable 1×4 one.[22]

However, the actual atomic structure of the 1×4 reconstructed (001) surface is still a matter of debate and several possible models have been hypothesized. Among these, the most widely accepted is the "add-molecule" model (ADM), obtained by adding rows of TiO_2 molecules on the (001) surface, which was originally theoretically predicted by Lazzeri and Selloni.[23] This proposed model was then supported by several experimental investigations which combined TEM with DFT calculations, clearly showing the typical tower-like configuration of the ADM reconstruction.[24,25] Nevertheless, other studies challenged this well-accepted ADM structure by proposing the "add-oxygen" model (AOM), which is obtained by adding oxygen adatoms to the ADM.[26] The two models share strong structural

[a]Department of Chemistry and NIS Centre, University of Torino, Via Giuria 7, 10125, Torino, Italy. E-mail: lorenzo.mino@unito.it

[b]UniTo-ITT JointLab, University of Torino, Via Quarello 15/A, 10135, Torino, Italy

† Electronic supplementary information (ESI) available. See DOI: https://doi.org/10.1039/d3ta06694k

analogies, therefore their differentiation based on electron microscopy results can be troublesome.[27–29]

In this work we aim to contribute to this ongoing debate, trying to elucidate the atomic structure of the (001) surface in shape-engineered TiO_2 anatase nanoparticles, after calcination to remove the capping agents employed during the hydrothermal synthesis. In particular, we compared two different kinds of shape-engineered anatase NPs: TiO_2 nano-sheets with dominant {001} facets and usual bipyramidal TiO_2 NPs, mainly exposing {101} facets. The former sample is synthesized using fluorides as shape controllers, while the latter is obtained using triethanolamine (see the Experimental section for the synthesis details). The surface structure of the samples was investigated by IR spectroscopy of CO adsorbed at very low temperature (60 K). Indeed, carbon monoxide is a very sensitive probe for the Ti^{4+} Lewis surface acid sites and the shift in its stretching frequency induced by the interaction with the metal oxide surface can provide very detailed information about the TiO_2 surface structure.[30–32] The interpretation of the experimental results was assisted by a systematic and thorough DFT simulation of the vibrational frequencies of the adsorbed CO molecules, considering all the possible different TiO_2 surface structures.

2. Experimental and computational details

2.1 Computational parameters

Periodic DFT calculations were carried out with the Vienna *Ab initio* Simulation Package, (VASP),[33,34] which uses projector-augmented wave (PAW) pseudopotentials[35] to describe the ionic cores and a plane wave basis set for the valence electrons. Geometry optimizations and frequency calculations were performed with the PBE-D2 method, which consists of the bare Perdew–Burke–Ernzerhof (PBE) functional[36] augmented with the *a posteriori* correction term D2 proposed by Grimme[37] to account for dispersive forces (missed partly in PBE). For the present work the energy cutoff of plane waves was set to 500 eV, the self-consistent field (SCF) iterative procedure was converged to a tolerance in total energy of $\Delta E = 10^{-5}$ eV. The tolerance on gradients for geometry optimizations was set to 0.01 eV $Å^{-1}$ for each atom in each direction. The *k*-point mesh was set to (8, 8, 8) for the bulk calculations. To simulate high-coverage regimes of the CO adsorption on the surface models the *k*-point mesh was set to (8, 8, 1), the *c* parameter being non-periodic for surface models, while for low-coverage regimes, as the cell size was doubled, the *k*-point mesh was reduced accordingly (4 4 1); as regards the reconstructed 001 surfaces, as they are already a 4×1 supercell (used for the high coverage CO adsorption), a *k*-point mesh equal to (2 8 1) was used, and (2 4 1) for the 4×2 supercell (used for the low coverage). The Monkhorst–Pack sampling of the Brillouin zone was used for the *k*-point mesh. The cell parameters of non-periodic direction have been chosen in order to have a vacuum space among fictitious replicas of almost 15 Å. Vibrational frequencies of a reduced Hessian matrix (*i.e.*, considering only the displacements of the CO atoms) were computed at the Γ point, by numerical differentiation of the analytical first derivatives, using the central difference formula (*i.e.*, two displacements for each atom in each direction).

For structure visualization and editing, and image rendering the MOLDRAW[38] and POVRAY[39] packages were used.

2.2 Surface DFT models

Starting from the crystal bulk structure of the TiO_2 anatase polymorph, we built crystalline periodic slab models for those surfaces which are particularly interesting for applications, which are the (101), (100) and (001) with thicknesses of 10 Å (3 layers), 13 Å (4 layers), and 22 Å (5 layers), respectively (see Fig. 1). Surface formation energies (E_s) were calculated according to the following formula:

$$E_s = \frac{E_{surf} - n_{Ti}E_{TiO_2,bulk} - (n_O - 2n_{Ti})\frac{1}{2}E_{O_2}}{2A}$$

where E_{surf} is the energy of the slab composed of n layers, $E_{TiO_2,bulk}$ the energy of the TiO_2 unit in the bulk structure normalized by the number of Ti atoms n_{Ti} in the slab (which corresponds to the number of TiO_2 units) to ensure the mass balance with respect to the considered surface, E_{O_2} the energy of the oxygen molecule to ensure the mass balance of non-stoichiometric surfaces with an excess of oxygen (n_O is the number of oxygen atoms in the slab), and A the surface area.

For the (001) surface three different models were adopted: the bare (001) as cut from the bulk structure (Fig. 1A), and two reconstructions, the one proposed by Lazzeri and Selloni[23] (hereafter referred to as 001_ADM, add-molecule model, Fig. 1B), and the more recent add-oxygen model[26] (hereafter referred to as 001_AOM, Fig. 1C). We highlight that the reconstructions have been applied on both top and bottom sides of the surface, thus ensuring the condition of zero dipole moment along the *z* non-periodic direction.

Binding energies were calculated with the following formula:

$$BE = (E_{TiO_2} + E_{CO}) - E_{CPLX}$$

where E_{CPLX} is the energy of the CO/TiO_2 complex, E_{TiO_2} and E_{CO} are the energies of the clean TiO_2 surface (either reconstructed or not) and of the isolated CO molecule in the gas phase, each one at its optimized geometry.

The cohesive energy (CE) of the CO bulk was calculated as:

$$CE = \frac{E_{CO}^{bulk} - E_{CO}^{mol}}{n}$$

where E_{CO}^{bulk} and E_{CO}^{mol} are the energies of the optimized bulk CO (crystalline or amorphous) and of the isolated CO molecule in the gas phase, and n the normalization factor given by the number of CO molecules in the periodic system.

All computed CO frequencies have been scaled to recover the systematic error due to the computational method and the harmonic approximation. The scaling factor has been calculated according to the following equation, considering CO in the gas phase:

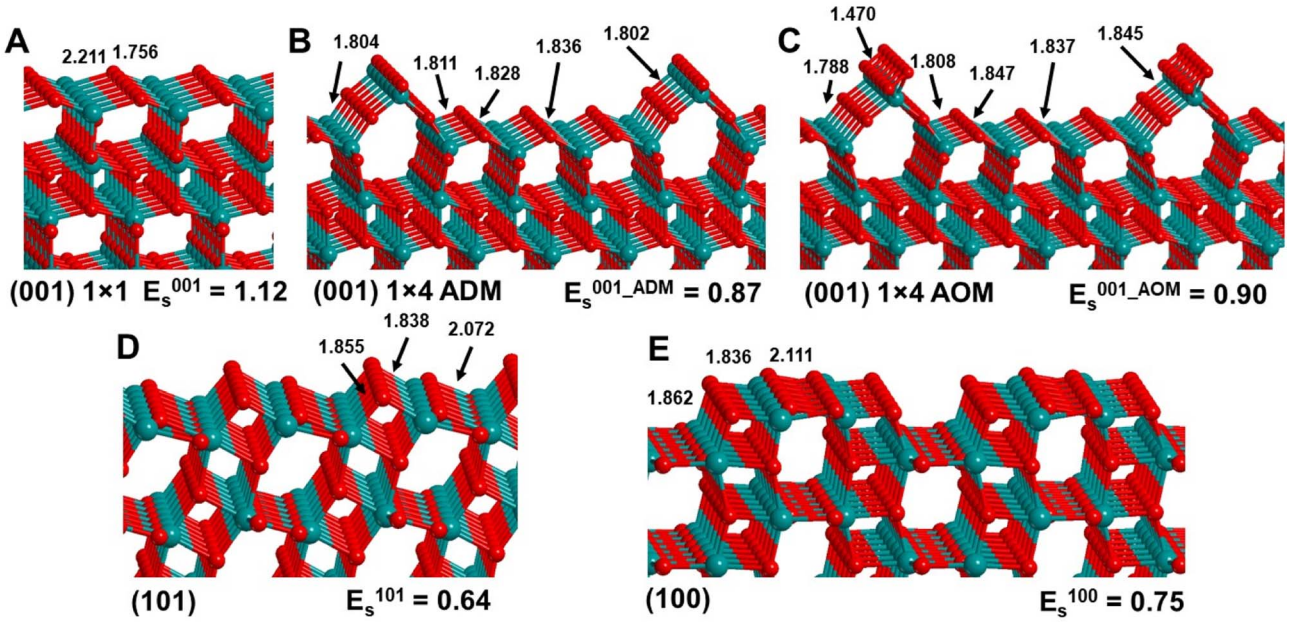

Fig. 1 PBE-D2 optimized geometries of bare TiO_2 surfaces. ADM and AOM stand for the add-molecule and add-oxygen (001) reconstructed models. Ti atoms in dark cyan, O atoms in red. Bond distances are indicated in Å and surface energies in J m^{-2}.

$$s_{CO} = \frac{\nu_{CO}^{exp}}{\nu_{CO}^{comp}} = \frac{2143\ cm^{-1}}{2124\ cm^{-1}} = 1.0088$$

2.3 Synthesis of shape-controlled TiO_2 nanoparticles

TiO_2 anatase nano-sheets, which preferentially expose {001} facets, were obtained using a solvothermal method. In a typical synthesis, $Ti(OBu)_4$ (Aldrich reagent grade 97%) was poured into a Teflon lined stainless steel reactor and then concentrated hydrofluoric acid (Aldrich reagent grade 47%) was added dropwise under stirring. The reactor was sealed and kept under stirring at 523 K for 24 hours. The resulting paste was centrifuged and washed several times with acetone to remove the residual organics and then with water (Milli-Q). The powder obtained by freeze-drying was then calcined in air at 873 K for 1 hour to remove all the fluorides employed as shape-controllers during the synthesis. The BET surface area of the final material is 34 $m^2\ g^{-1}$.

TiO_2 anatase bipyramids, which preferentially expose {101} facets, were obtained by forcing the hydrolysis of a 40 mM aqueous solution of $Ti(TeoaH)_2$ complex (TeoaH = triethanolamine; initial pH 10), carried out by hydrothermal treatment at 453 K for 90 hours in an autoclave. The material was calcined in air at 873 K for 1 hour. The BET surface area of the final material was 37 $m^2\ g^{-1}$. Further details on the preparation and characterization of these nano-sheets and bipyramidal nanoparticles can be found in our previous publications.[10,19]

2.4 Characterization techniques

The infrared spectra were recorded on a Bruker Equinox 55 FTIR spectrometer, equipped with an MCT cryogenic detector, with the sample compartment modified to accommodate a properly modified closed circuit liquid helium Oxford CCC 1204 cryostat allowing infrared investigations of species adsorbed under controlled temperature (between 300 and 14 K) and pressure conditions. For each spectrum, 128 interferograms recorded at 2 cm^{-1} resolution were typically averaged. Before CO adsorption the TiO_2 samples, in the form of thin self-supporting pellets suitable for transmission FTIR measurements, were outgassed under high vacuum (residual pressure $<10^{-4}$ mbar) at 873 K. The thermal treatment was followed by an oxidation step at 873 K to avoid the presence of oxygen vacancies.

High resolution transmission electron microscopy images were obtained, after dispersing the materials on lacey carbon Cu grids, using a JEOL 3010 UHR microscope operated at 300 kV. SEM images were obtained with a Zeiss Supra 40 scanning electron microscope (Carl Zeiss, Oberkochen, Germany), equipped with a Schottky field emitter, operated at 10 kV.

X-ray powder diffraction patterns were recorded with a PANalytical X'Pert Pro powder diffractometer, equipped with an X'Celerator detector, using Cu Kα radiation generated at 45 kV and 40 mA. The 2θ range was from 10° to 80° with a step size of 0.01° and a counting time of 0.6 s per point.

3. Results and discussion

As mentioned in the Introduction, before investigating the TiO_2 surface structure, the samples were thermally treated in air at 873 K, with the usual procedure adopted to remove the shape controllers employed in the hydrothermal synthesis. The X-ray diffraction patterns (Fig. S1†) confirm that both samples are pure anatase TiO_2 and, thus, that the calcination does not induce anatase to rutile phase transitions.[40]

Representative electron micrographs of the cleaned samples are reported in Fig. 2. The NPs obtained adding triethanolamine as the shape controller (bipy, Fig. 2A and B) appear as slightly truncated bipyramids, dominated by {101} facets (~90%), as quantitatively determined in previous studies.[19,41] Conversely, the NPs synthesized using fluorides as capping agents (n-sh, Fig. 2C and D) show the expected nano-sheet shape, exposing ~60% of {001} facets after calcination at 873 K.[19,41] The assignment of the most abundant exposed facet in the n-sh sample to the anatase (001) is confirmed by HR-TEM images (Fig. 2D) where properly oriented NPs exhibit lattice fringes with a spacing of 0.237 nm, typical of the (004) family of lattice planes (d_{004} = 0.2378 nm according to ICDD PDF 00-021-1272), which are parallel to the NP basal facets.

The surface of the two materials was then investigated at the molecular level by IR spectroscopy employing carbon monoxide as the probe molecule. The samples were previously outgassed at 873 K to completely remove adsorbed contaminants, water molecules and nearly all hydroxyl groups, and then oxidized to obtain stoichiometric TiO_2 (see Experimental and computational details in the ESI†). From Fig. 3, we can see that, at the maximum CO coverage, the spectrum of the bipy NPs (black curve in Fig. 3A) is dominated by a peak at 2178 cm^{-1}. Minor bands are centred at 2164, 2156 and 2139 cm^{-1}. The latter one can be readily assigned to physisorbed CO forming a surface multilayer and, as expected, is the first to disappear upon decreasing CO coverage (grey to red curves in Fig. 3). The other bands are more resistant to outgassing, in agreement with their higher hypsochromic shift with respect to CO in the gas phase ($\nu_{CO\ gas}$ = 2143 cm^{-1}). Indeed, the CO stretching frequency is directly related to the electrophilicity and Lewis acidity of the Ti adsorption site. Moreover, all the signals blue-shift while decreasing the coverage because the CO stretching frequency is also significantly influenced by the static and dynamic

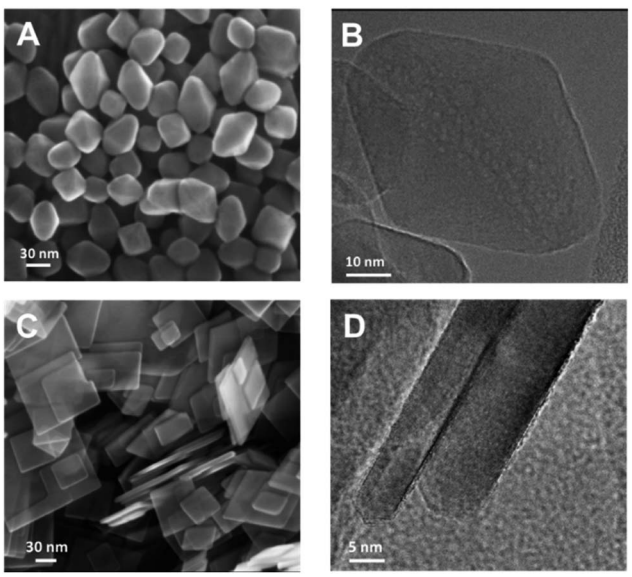

Fig. 2 SEM and HR-TEM images of the bipy (A and B) and n-sh (C and D) TiO_2 samples.

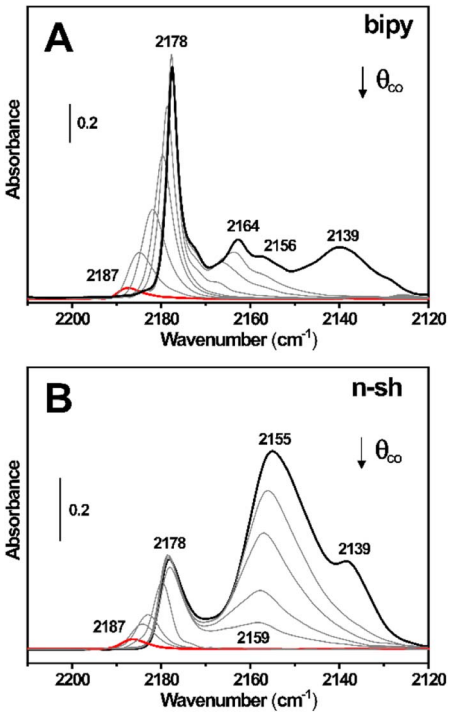

Fig. 3 FT-IR spectra, recorded at 60 K, of CO adsorbed at decreasing coverages on the bipy (A) and n-sh (B) TiO_2 samples previously outgassed at 873 K. The black curve refers to maximum CO coverage while spectra from grey to red to progressive CO outgassing.

interactions among the adsorbed molecules. For instance, the position of the main peak shifts from 2178 to 2187 cm^{-1} moving from a monolayer of interacting CO to isolated CO molecules (*i.e.*, from θ_{CO} = 1 to $\theta_{CO} \rightarrow 0$). Regarding the n-sh sample (Fig. 3B), we can immediately note that the intensity of the signal at 2178 cm^{-1} considerably decreases and the spectrum at the maximum CO coverage (black curve in Fig. 3B) is now dominated by the band at 2155 cm^{-1}, which shifts till 2159 cm^{-1} at lower CO coverage. It is worth noting that the band at 2155 cm^{-1} almost completely disappears if the adsorption experiment is performed at higher temperature (*e.g.*, at liquid N_2 temperature, often employed in low temperature IR studies).

From the previous discussion it is clearly seen that a thorough analysis, assisted by DFT simulations, of the position of the different CO bands and of their shift with coverage can provide very detailed information about the properties and spatial distribution of the Ti surface sites and, hence, about the structure of the different adsorbing facets. We started our DFT investigation considering all the most stable TiO_2 surfaces which should appear in both bipy and n-sh TiO_2 samples, namely (001), (101) and (100), as shown in Fig. 1. For the (001), besides the bulk-truncated 1 × 1 model, we considered both ADM (Fig. 1B) and AOM (Fig. 1C) reconstructions. In particular, the ADM is obtained from the bare (001) surface where for every four repeat units along the [010] direction, another TiO_2 unit is added on top of the surface, thus forming an infinite row of TiO_2 units, which make this model still stoichiometric. The AOM model is the same as that of ADM, but with an excess of

oxygen atoms, *i.e.*, another oxygen atom (non-stoichiometric) is added on the top of the TiO_2 row of the ADM (see Fig. S2†).

According to our results obtained with the present methodology, the surface energy ranking is as follows: $E_s^{101} = 0.64$, $E_s^{100} = 0.75$, and $E_s^{001} = 1.12$ J m^{-2}, and, for the reconstructed ones, E_s001_ADM = 0.87, and E_s001_AOM = 0.90 J m^{-2}, which is in qualitative agreement with previous studies.[28] From one model to another, the surface energy changes according to the acidity (Ti_{5c}) and basicity (O_{2c}) of the sites due to the bulk cut along the specific crystallographic directions. As reported in Fig. 1, bulk Ti–O bonds usually present a typical length of ~2.1 Å, while Ti–O bonds in the outermost part of the surface are about 1.8–1.9 Å. This is not valid for the (001) bare surface, whose Ti–O bonds, equal by symmetry, deeply change once the symmetry is removed, thus creating two different Ti–O bonds (2.21 and 1.76 Å). In the reconstructed models, this discrepancy between two bonds, that in principle should be indistinguishable, is almost lost, the Ti–O bond lengths being more uniformly distributed (around 1.79–1.84 Å), and this contributes to give more stability to the reconstructed (001) models.

Fig. 4 shows the modelling of CO adsorption on the different TiO_2 surfaces. Both low (LC) and high (HC) CO coverage regimes have been studied and Table 1 summarizes the binding energies of CO with its corresponding geometrical and vibrational features for all models. As a test, for the (101) surface also a very low coverage regime was explored (101_LC3 in Table 1), highlighting that the CO stretching frequency is not further changing by lowering the θ_{CO} from 0.25 to 0.11.

CO presents a small dipole moment ($C^{\delta-} \rightarrow O^{\delta+}$) and, overall, the molecule is a quadrupole. The two negative poles are localized on the C and O atoms which, in their most representative Lewis resonance form, have a lone electron pair on them ($|C^{-}\equiv O^{+}|$), while the bond region represents the positive "belt", as shown in Fig. S3.† The methodology presented in the Computational details section gives a reasonable description of these features,[42] predicting an electric dipole moment of 0.203 D, in good accordance with the experimental value of 0.122 D,[43] considering also the small absolute value, which many reliable methodologies tend to reverse. Following the colours of Fig. S3,† one can expect two kinds of favourable

Table 1 Surface coverage (θ), scaled frequencies (ν), binding energies (BE, or cohesive energy in the case of bulk CO) and geometric data for all the systems studied. $\Delta\nu$ refers to the shift of the computed frequency of the CO/TiO_2 system with respect to the computed CO frequency in the gas phase (in parenthesis the experimental shifts obtained from Fig. 3 are reported). HC and LC stand for high- and low-coverage regimes. ADM and AOM are the (001) add-molecule and add-oxygen reconstructions, respectively. CO cry and am are the crystalline and amorphous carbon monoxide bulk structures

System	θ	Scaled ν (cm^{-1})	$\Delta\nu$ (cm^{-1})	BE (kJ mol^{-1})	Ti–C (Å)	C–O (Å)
101_HC	1	2177	+34 (+35)	36.2	2.511	1.140
101_LC2	0.25	2186	+43 (+44)	38.5	2.491	1.138
101_LC3	0.11	2186	+43 (+44)	39.8	2.493	1.138
100_HC	1	2165	+22 (+21)	31.2	2.480	1.141
100_LC	0.125	2177	+34 (+30)	36.4	2.448	1.139
001_HC	1	2150	+7 (+12)	27.8	2.418	1.143
001_LC	0.25	2155	+12 (+16)	39.1	2.341	1.142
ADM_HC	1	2138	−5 (+12)	35.3	2.367	1.144
ADM_LC	0.5	2152	+9 (+16)	40.8	2.314	1.142
AOM_HC	1	2156	+13 (+12)	18.6	2.844	1.142
AOM_LC	0.5	2161	+18 (+16)	22.7	2.665	1.140
CO cry	—	2145	+2 (−4)	8.6	—	—
CO am	—	2142	−1 (−4)	7.8	—	—

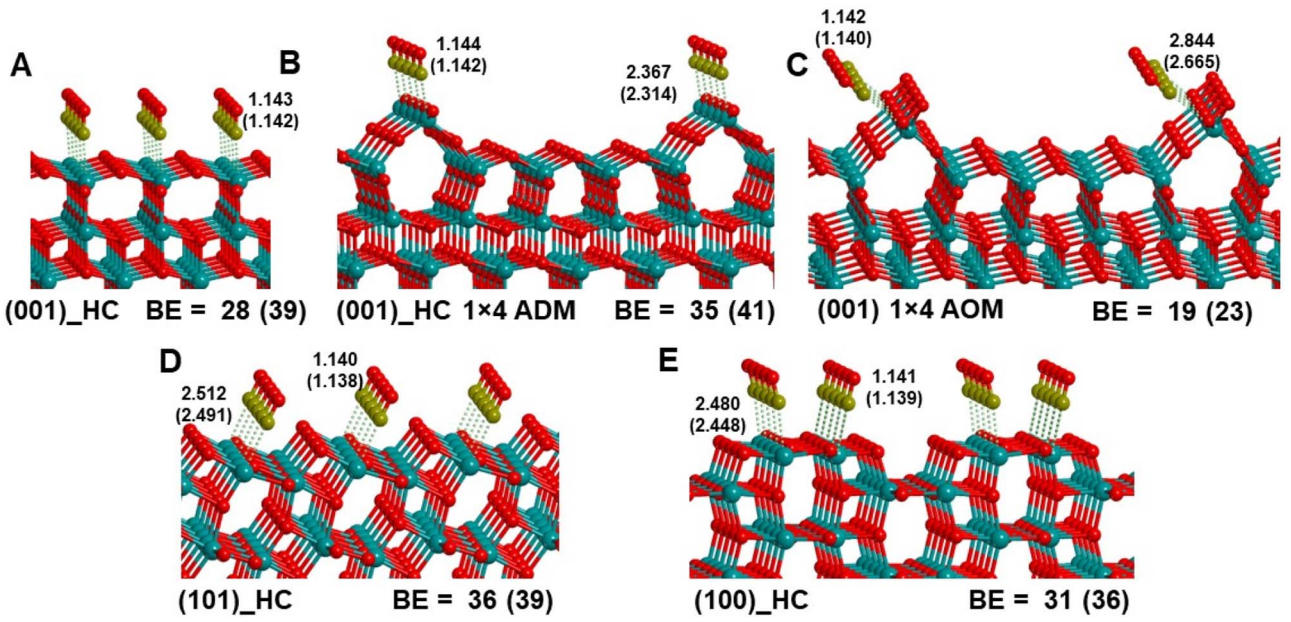

Fig. 4 PBE-D2 optimized geometries of CO adsorbed at high coverage on the different TiO_2 surfaces. Ti atoms in dark cyan, O atoms in red, C atoms in ochre. Bond distances are indicated in Å and binding energies (BE) in kJ mol^{-1}. In parenthesis the bond distances and BE values for the low coverage CO conditions are reported (see also Table 1).

electrostatic interactions: the strongest one where the C atom of the CO donates its electron lone pair to Ti_{5c} atoms of the TiO_2 surface, and a very weak interaction of the electron rich part of the surface (O_{2c}) with the positive "belt" of the CO. The former is responsible for the blue shift of the CO stretching frequency with respect to the gas phase one, due to the repulsive potential of the CO vibration against a rigid surface (wall effect), while the latter produces a weakening of the CO bond and, accordingly, a red shift of its stretching frequency due to lateral interactions among CO molecules, in the case of monolayer and multilayer regimes.[7,44]

Comparing the experimental and computational results, we can unambiguously attribute the main peak in the IR spectrum of bipy TiO_2 sample, which is centred at 2178 cm^{-1} at maximum CO coverage (Fig. 3A, black curve), to the CO adsorbed on the (101) surface. From our calculations, indeed, the CO monolayer (101_HC) vibrates at a frequency of 2177 cm^{-1} ($\Delta\nu$ = +34 cm^{-1} with respect to the gas phase value). This assignment is also in agreement with literature results obtained by infrared reflection absorption spectroscopy on anatase single crystals exposing the (101) surface.[45,46] Our computational setup is also satisfactory reproducing the band blue-shift observed in the CO desorption process since the isolated CO molecule adsorbed on the (101) surface has a calculated frequency of 2186 cm^{-1} ($\Delta\nu$ = +44 cm^{-1}) compared to an experimental value of 2187 cm^{-1} when $\theta_{CO} \rightarrow 0$. The band at 2164 cm^{-1} finds a good match with the CO adsorbed on the (100) surface at $\theta_{CO} = 1$ (2165 cm^{-1} simulated, $\Delta\nu$ = +22 cm^{-1}). Also in this case, during the outgassing the signal blueshifts and its final position (>2170 cm^{-1}) is difficult to precisely detect as it tends to collapse within the main peak at 2178 cm^{-1}. Our calculations indeed predict a CO stretching frequency of 2177 cm^{-1} when the coverage is simulated at isolated adsorption regime on the (100) surface, very similar to the CO monolayer adsorption on the (101).

The remaining band, shifting from 2155 to 2159 cm^{-1} with coverage, can be ascribed to CO on the (001) surface. From the experimental spectra of Fig. 3 this assignment is intuitive, since its relative intensity increases from the bipy sample (Fig. 3A), dominated by the (101) surface, to the n-sh sample (Fig. 3B), dominated by the (001) surface.

The results of the simulations on the bulk-truncated (001) surface are not too far from the experiment, *i.e.*, 2150 and 2155 cm^{-1} for the high and low coverage, respectively. However, in this case the binding energies do not reflect the outgassing behaviour since in the n-sh sample (Fig. 3B) the CO is completely desorbed from the (001) surfaces, while the signal of the (101) at 2178 cm^{-1} is still unchanged, but the binding energies of 101_LC and 001_LC are very similar (BE_{101_LC} = 38.5/39.8 kJ mol^{-1} and BE_{001_LC} = 39.1 kJ mol^{-1}). To find a better correspondence with the experimental data we also therefore explored the above-mentioned (001) reconstructions. In our case, the ADM model, which is the most widely accepted (001) reconstruction, fits worse with the experiment than the bare (001). Indeed, at high coverage the CO stretching frequency even red-shifts (−5 cm^{-1}), and also at low coverage the difference with respect to the experiment is larger than for the other (001) models, *i.e.*, $\Delta\nu^{EXP}$ = 2159 cm^{-1}, $\Delta\nu^{CALC}$ = 2152 cm^{-1}. Moreover, the binding energies are too high to match with the experimental results (BE_{ADM_HC} = 35.3 kJ mol^{-1} and BE_{ADM_LC} = 40.8 kJ mol^{-1}). Finally, also the AOM model was tested, and in this case the difference between experimental and computed frequencies is similar to the one calculated for the (101) and (100) surfaces (*i.e.*, +1/+2 cm^{-1}). Moreover, also the BEs are clearly lower with respect to the other (001) surface models (BE_{AOM_HC} = 18.6 kJ mol^{-1} and BE_{AOM_LC} = 22.7 kJ mol^{-1}), thus explaining the observed easier desorption of the CO from the {001} facets.

Finally, the experimental peak at 2139 cm^{-1} can be ascribed to the formation of a CO multilayer, simulated with a 3D periodic cell of the CO bulk structure, either crystalline or amorphous (see Fig. S4†). The results show that in both cases the shift with respect to the gas phase molecule is very low: in the crystalline case we obtained a small blue-shift (+2 cm^{-1}), while in the amorphous one a minimum red-shift (−1 cm^{-1}). Both seem to be acceptable, also from the point of view of the binding energies which are very low (about 8 kJ mol^{-1}), thus confirming the fast removal of the CO multilayer during the outgassing procedure.

On the basis of the above discussion, we therefore propose that the AOM should be considered as the best model to simulate the reconstruction of the bare (001) surface at high temperature under oxidizing conditions. We would also like to note that, although the AOM surface energy is slightly higher than the ADM one, the calculation of such small energy differences between stoichiometric and non-stoichiometric structures may be tricky. In particular, for these specific systems there are two main sources of errors: (i) the mass balance to calculate the surface energy of AOM, which is ensured assuming $E_O = \frac{1}{2}E_{O_2}$, and (ii) the intrinsic difficulties in calculating the absolute energy of the O_2 molecule, a well-known multi-reference problem in computational chemistry, here treated at the PBE level for consistency with the other calculations for the surfaces. Therefore, to further assess the reliability of the calculated surface energy for the AOM, we tried to estimate the error in the PBE absolute energy of the O_2 molecule using the following reaction:

$$CH_4 + 2O_2 \rightleftarrows CO_2 + H_2O$$

The reaction energy was calculated at the same level of theory used in the paper (*i.e.*, PBE-D2) and with the golden standard CCSD(T)/aug-cc-pv5z, obtaining −735 and −811 kJ mol^{-1}, respectively. We assumed that CH_4, CO_2, and H_2O are reasonably described by PBE and, therefore, that the error is dominated by O_2. In this way, we determined a correction of 38 kJ mol^{-1} per O_2 molecule which was added to the O_2 PBE total energy to calculate the new corrected AOM surface energy which is 0.85 J m^{-2}. This value is now slightly lower than the calculated surface energy for the ADM surface, which is 0.87 J m^{-2}. These considerations further show that the stability of the AOM and ADM reconstructions is similar and, thus, that only a synergistic comparison between simulation and experiments can provide reliable conclusions about this complex topic.

4. Conclusions

In this paper, we contributed to the lively debate about the actual atomic structure of the (001) anatase surface focusing on shape-engineered TiO_2 nanoparticles thermally treated in air to remove the capping agents (*i.e.*, fluorides) employed for the synthesis. While a huge number of experimental and computational studies have been performed on TiO_2 single crystal surfaces, the application of a surface science approach to anatase nanoparticles is much more limited. IR spectroscopy of CO adsorbed turned out to be a perfect tool to investigate the structure of the exposed oxide facets. The use of a cryostat to reach very low temperatures (60 K) was crucial to study the interaction of CO with {001} facets since at higher temperatures the adsorption is negligible. This spectroscopic approach can provide quantitative information about the fraction of the different exposed facets, overcoming for instance the statistical limitations of HR-TEM analysis.

The comparison of the experimental IR spectra with systematic DFT calculations allowed us to highlight that, as expected, shape-engineered bipyramidal NPs are dominated by the (101) surface, but small fractions of {001} and {100} facets are also present (the latter not present in the Wulff construction for anatase). Conversely, in shape-engineered anatase nanosheet NPs the most intense IR peak is ascribed to CO adsorption on {001} facets with a smaller band due to the {101} and no signals associated to {100} facets. A careful analysis of the DFT models for the different possible reconstructions of the (001) surface allowed us to conclude that our experimental results can be better explained by the "add-oxygen" model (AOM) and not by the most commonly proposed "add-molecule" model (ADM). We can thus infer that, during the thermal treatment in oxygen, which is the standard procedure to eliminate the capping agents employed in the synthesis of shape-controlled NPs, the {001} facets undergo a reconstruction leading to the AOM structure. Conversely, annealing processes under ultra-high vacuum conditions, usually employed in surface science studies, likely lead to the most frequently reported ADM reconstruction. Our findings represent an important basis for future experimental and computational investigations, showing that the AOM reconstruction is the most appropriate model to describe the reactivity and properties of the {001} facets in shape-engineered TiO_2 nanoparticles after the elimination of the capping agents.

Conflicts of interest

There are no conflicts to declare.

Acknowledgements

This work has been partially supported by the Spoke 7 "Materials and Molecular Sciences" of ICSC – Centro Nazionale di Ricerca in High-Performance Computing, Big Data and Quantum Computing, funded by European Union – NextGenerationEU. The authors acknowledge support from the Project CH4.0 under the MUR program "Dipartimenti di Eccellenza 2023–2027" (CUP: D13C22003520001).

References

1 X. Chen and S. S. Mao, *Chem. Rev.*, 2007, **107**, 2891–2959.
2 M. A. Henderson, *Surf. Sci. Rep.*, 2011, **66**, 185–297.
3 Q. Guo, C. Y. Zhou, Z. B. Ma, Z. F. Ren, H. J. Fan and X. M. Yang, *Chem. Soc. Rev.*, 2016, **45**, 3701–3730.
4 L. Mino, F. Cesano, D. Scarano, G. Spoto and G. Martra, *Res. Chem. Intermed.*, 2019, **45**, 5801–5829.
5 G. Liu, J. C. Yu, G. Q. Lu and H. M. Cheng, *Chem. Commun.*, 2011, **47**, 6763–6783.
6 M. H. Huang, G. Naresh and H. S. Chen, *ACS Appl. Mater. Interfaces*, 2018, **10**, 4–15.
7 L. Mino, A. M. Ferrari, V. Lacivita, G. Spoto, S. Bordiga and A. Zecchina, *J. Phys. Chem. C*, 2011, **115**, 7694–7700.
8 H. G. Yang, C. H. Sun, S. Z. Qiao, J. Zou, G. Liu, S. C. Smith, H. M. Cheng and G. Q. Lu, *Nature*, 2008, **453**, 638–641.
9 W. J. Ong, L. L. Tan, S. P. Chai, S. T. Yong and A. R. Mohamed, *Nanoscale*, 2014, **6**, 1946–2008.
10 F. Pellegrino, F. Sordello, L. Mino, C. Minero, V. D. Hodoroaba, G. Martra and V. Maurino, *ACS Catal.*, 2019, **9**, 6692–6697.
11 C. P. Sajan, S. Wageh, A. A. Al-Ghamdi, J. G. Yu and S. W. Cao, *Nano Res.*, 2016, **9**, 3–27.
12 S. M. Wu and P. Schmuki, *Energy Technol.*, 2023, 2300052, DOI: **10.1002/ente.202300052**.
13 T. R. Gordon, M. Cargnello, T. Paik, F. Mangolini, R. T. Weber, P. Fornasiero and C. B. Murray, *J. Am. Chem. Soc.*, 2012, **134**, 6751–6761.
14 M. V. Dozzi, M. Montalbano, G. Marra, L. Mino and E. Selli, *Mater. Today Chem.*, 2021, **22**, 100624.
15 F. Pellegrino, E. Morra, L. Mino, G. Martra, M. Chiesa and V. Maurino, *J. Phys. Chem. C*, 2020, **124**, 3141–3149.
16 M. Bellardita, C. Garlisi, L. Y. Ozer, A. M. Venezia, J. Sa, F. Mamedov, L. Palmisano and G. Palmisano, *Appl. Surf. Sci.*, 2020, **510**, 145419.
17 C. Adler, D. Mitoraj, I. Krivtsov and R. Beranek, *J. Chem. Phys.*, 2020, **152**, 10.
18 M. Maisano, M. V. Dozzi, M. Coduri, L. Artiglia, G. Granozzi and E. Selli, *ACS Appl. Mater. Interfaces*, 2016, **8**, 9745–9754.
19 L. Mino, F. Pellegrino, S. Rades, J. Radnik, V. D. Hodoroaba, G. Spoto, V. Maurino and G. Martra, *ACS Appl. Nano Mater.*, 2018, **1**, 5355–5365.
20 X. H. Yang, Z. Li, C. H. Sun, H. G. Yang and C. Z. Li, *Chem. Mater.*, 2011, **23**, 3486–3494.
21 S. Selcuk and A. Selloni, *J. Phys. Chem. C*, 2013, **117**, 6358–6362.
22 W. T. Yuan, Y. Wang, H. B. Li, H. L. Wu, Z. Zhang, A. Selloni and C. H. Sun, *Nano Lett.*, 2016, **16**, 132–137.
23 M. Lazzeri and A. Selloni, *Phys. Rev. Lett.*, 2001, **87**, 266105.
24 W. T. Yuan, B. E. Zhu, X. Y. Li, T. W. Hansen, Y. Ou, K. Fang, H. S. Yang, Z. Zhang, J. B. Wagner, Y. Gao and Y. Wang, *Science*, 2020, **367**, 428–430.
25 K. Fang, G. X. Li, Y. Ou, W. T. Yuan, H. S. Yang, Z. Zhang and Y. Wang, *J. Phys. Chem. C*, 2019, **123**, 21522–21527.

26 Y. Wang, H. J. Sun, S. J. Tan, H. Feng, Z. W. Cheng, J. Zhao, A. D. Zhao, B. Wang, Y. Luo, J. L. Yang and J. G. Hou, *Nat. Commun.*, 2013, **4**, 2214.
27 G. X. Li, K. Fang, Y. Ou, W. T. Yuan, H. S. Yang, Z. Zhang and Y. Wang, *Prog. Nat. Sci.*, 2021, **31**, 1–13.
28 Y. L. Shi, H. J. Sun, W. A. Saidi, M. C. Nguyen, C. Z. Wang, K. M. Ho, J. L. Yang and J. Zhao, *J. Phys. Chem. Lett.*, 2017, **8**, 1764–1771.
29 H. J. Sun, W. C. Lu and J. Zhao, *J. Phys. Chem. C*, 2018, **122**, 14528–14536.
30 K. Hadjiivanov, J. Lamotte and J. C. Lavalley, *Langmuir*, 1997, **13**, 3374–3381.
31 L. Mino, G. Spoto, S. Bordiga and A. Zecchina, *J. Phys. Chem. C*, 2013, **117**, 11186–11196.
32 C. Woll, *ACS Catal.*, 2020, **10**, 168–176.
33 G. Kresse and J. Furthmuller, *Comput. Mater. Sci.*, 1996, **6**, 15–50.
34 G. Kresse and J. Furthmuller, *Phys. Rev. B: Condens. Matter Mater. Phys.*, 1996, **54**, 11169–11186.
35 G. Kresse and D. Joubert, *Phys. Rev. B: Condens. Matter Mater. Phys.*, 1999, **59**, 1758–1775.
36 J. P. Perdew, K. Burke and M. Ernzerhof, *Phys. Rev. Lett.*, 1996, **77**, 3865–3868.
37 S. Grimme, *J. Comput. Chem.*, 2006, **27**, 1787–1799.
38 P. Ugliengo, D. Viterbo and G. Chiari, *Z. Kristallogr.*, 1993, **207**, 9–23.
39 **https://www.povray.org**.
40 M. J. Uddin, F. Cesano, A. R. Chowdhury, T. Trad, S. Cravanzola, G. Martra, L. Mino, A. Zecchina and D. Scarano, *Front. Mater.*, 2020, **7**, 192.
41 Y. Wang, L. Mino, F. Pellegrino, N. Homs and P. Ramirez de la Piscina, *Appl. Catal. B: Environ.*, 2022, **318**, 121783.
42 G. E. Scuseria, M. D. Miller, F. Jensen and J. Geertsen, *J. Chem. Phys.*, 1991, **94**, 6660–6663.
43 J. S. Muenter, *J. Mol. Spectrosc.*, 1975, **55**, 490–491.
44 G. Pacchioni, A. M. Ferrari and P. S. Bagus, *Surf. Sci.*, 1996, **350**, 159–175.
45 M. C. Xu, Y. K. Gao, E. M. Moreno, M. Kunst, M. Muhler, Y. M. Wang, H. Idriss and C. Woll, *Phys. Rev. Lett.*, 2011, **106**, 138302.
46 M. Setvin, M. Buchholz, W. Y. Hou, C. Zhang, B. Stoger, J. Hulva, T. Simschitz, X. Shi, J. Pavelec, G. S. Parkinson, M. C. Xu, Y. M. Wang, M. Schmid, C. Woll, A. Selloni and U. Diebold, *J. Phys. Chem. C*, 2015, **119**, 21044–21052.